# Crumpling an elastoplastic thin sphere

Hung-Chieh Fan Chiang,[1] Li-Jie Chiu,[1] Hsin-Huei Li,[1] Pai-Yi Hsiao,[2] and Tzay-Ming Hong[1,*]

[1]*Department of Physics, National Tsing Hua University, Hsinchu 30013, Taiwan, Republic of China*

[2]*Department of Engineering and System Science, National Tsing Hua University, Hsinchu 30013, Taiwan, Republic of China*

(Received 22 November 2019; revised 31 March 2020; accepted 23 December 2020; published 12 January 2021)

The phenomenon of crumpling is common in nature and our daily life. However, most of its properties, such as the power-law relation for pressure versus density and the ratio of bending and stretching energies, as well as the interesting statistical properties, were obtained by using flat sheets. This is in contrast to the fact that the majority of crumpled objects in the real world are three-dimensional. Notable examples are car wreckage, crushed aluminum cans, and blood cells that move through tissues constantly. In this work, we did a thorough examination of the properties of a crumpled spherical shell, hemisphere, cube, and cylinder via experiments and molecular-dynamics simulations. Physical arguments are provided to understand the discrepancies with those for flat sheets. The root of this disparity is found to lie less in the nonzero curvature, sharp edges and corner, and open boundary than in the dimensionality of the sample.

DOI: 10.1103/PhysRevE.103.012209

## I. INTRODUCTION

The squeezing of an object occurs quite often in daily life, e.g., crumpling a piece of paper or crushing an aluminum can. We all know that wrinkled paper consists mainly of ridges and vertices, whereas a squeezed can or a virus exhibits dents and buckling on its surface [1]. Similar deformation patterns can also be observed on a polymer gel that undergoes extensive swelling [2]. In spite of this obvious difference in the shape of deformation, most research has been dedicated to studying the former, i.e., flat sheets [3–6]. Many interesting properties have been reported. Among them are (i) the size $R$ of a crumpled sheet versus applied pressure $P$ obeys a power-law relation with an exponent independent of thickness $t$ and original size $R_0$ [7–11], but varying with Young's modulus $Y$ [12,13]. (ii) As $R$ decreases, ordered domains of layers are formed in the interior [14], and this change of morphology is intimately correlated with the breakdown of a power law, which is replaced by a universal behavior where different data sets can be mapped onto a master curve [13]. (iii) Another property is energetic scaling, including the ratio of stretching and bending energies $E_b/E_s = 5$ and the storage energy $E(\ell) \propto \ell^{1/3}$ for a ridge of length $\ell$ [15,16]. (iv) In addition to comparing the buildup of stiffness from crumpling to repeated folding, Deboeuf *et al.* [17] found a similar analogy pertaining to how a layer number increases with compaction, a view that was confirmed by later studies [18,19]. (v) Friction [20] affects the relaxation process of a crumpled flat sheet, and the degree of wrinkling on a curved surface determines its friction [21].

In Secs. II–VI we revisit the crumpling of a spherical thin shell via experiments and molecular-dynamics (MD) simulations. To clarify whether the source of the new properties comes from the nonzero curvature, the fact that the sample is three-dimensional, or even the existence of an open boundary, we also studied the behavior of a crumpled hemisphere, cube, and cylinder in Sec. VII. A conclusion and discussions are presented in the final section.

## II. SAMPLE AND EXPERIMENTAL SETUP

In previous experiments [12,13], high-density polyethylene (PE) films and aluminum foils were often used. But both are hard to come by in the form of a uniform sphere without sutures. Finding a suitable sample turned out to be the first major obstacle we had to overcome. It was only after several unsuccessful attempts that we were left to resort to homemade paper shells and polyvinyl chloride (PVC) balls. Pulp was prepared by cutting A4 paper of 80 gsm into pieces and adding them to a blender with water. We then spread the pulp uniformly on several strainers and baked them in an oven at 300 °C for 15 min. Finally, two of these hemispheres were combined and superglued into a ball. Our samples are characterized by $Y \sim 9.42 \pm 0.40$ GPa, yield strain $\sim 0.737 \pm 0.050$, and arithmetic average roughness [22] 0.0445 mm. To determine the degree of uniformity, we measured the thickness by a caliper at several locations along the edge of the hemisphere. The error $\Delta t$ was kept below 0.005 mm for $t = 0.22$ mm. For comparison, we also tested another more elastic material, i.e., PVC balls with $Y \sim 3.38 \pm 0.51$ MPa. Unlike Polycarbonate//Polydimethylsiloxane (PC/PDMS) in Ref. [23], there is little adhesion for the surface of our paper shell. To make sure our sample is reliable, we ran a parallel test on flat paper sheets made of the same pulp. Both mechanical and statistical properties are consistent with previous results [12,13,16]. Data can be found in the supplemental material (SM) [24].

To achieve the effect of three-dimensional (3D) crumpling, we wrap the sample using condoms and connect it to the outside of a high-pressure chamber, shown in Figs. 1(a)

*ming@phys.nthu.edu.tw

 

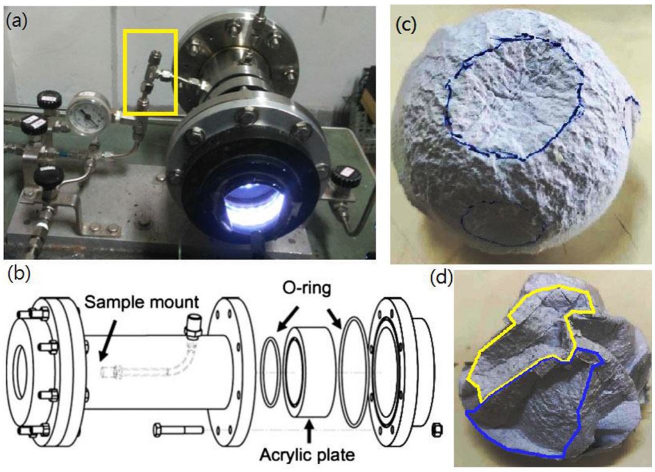


FIG. 1. Panels (a) and (b) show the high-pressure chamber where the yellow cube indicates a steel tube that connects the sample to the outside. Photos (c) and (d) show craters with a circular and polygonal boundary in the early and late states of a crumpled shell.

and 1(b), filled with nitrogen gas and with a leakage rate of maximum 71.7 mL/h. The crumple process is continued up to a pressure of 120 psi. The condom serves two purposes. First, a membrane will not crumple in high-pressure gas due to the lack of pressure difference. To achieve this, the condom functions as a boundary to separate the injected nitrogen gas from the sample inside. The interior of the condom is kept at the standard pressure by connecting a 6-mm-diam PE tube to the exterior of the pressure chamber. Why not use the much cheaper plastic wrap? Ambient pressure tends to intensify the local structure of the crumpled ball and render its surface increasingly thorny. The excellent toughness of the condom against piercing became its advantage. Since the thickness of a condom is less than the radius of most compact balls, the error that the condom might cause to the estimation of the latter is negligible. The surface tension of a condom is likely to prevent it from slipping because the volume of a crumpled ball at 120 psi is still five to six times larger than the initial volume of a condom.

## III. MECHANICAL RESPONSE

In the early days when a high-pressure chamber was designed to replace human hands for the study of three-dimensional crumpling [12], we noticed that a crumpled ball tends to deviate from a spherical shape in addition to the aforementioned spikes and deep valleys on its surface. Although less accurate at calibrating the crumple force, hand-crumpled sheets [9,25] are now believed to produce reasonably correct mechanical response by taking the mean of many measurements.

For our crumpled ball, the radius $R$ is determined by averaging over the cross sections from three perpendicular directions [12]. As shown in Fig. 2(a), the relations between dimensionless pressure $P/Y$ and $R/R_0$ for pulp and PVC balls are qualitatively similar in that they can be separated into three regimes [26]. To compare with flat sheets, we tried to fit $R/R_0 > 0.80$ by a power law, $P/Y \sim (R/R_0)^{-\alpha}$ with $\alpha \sim 4.6$. In this Regime 1, shallow craterlike indentations

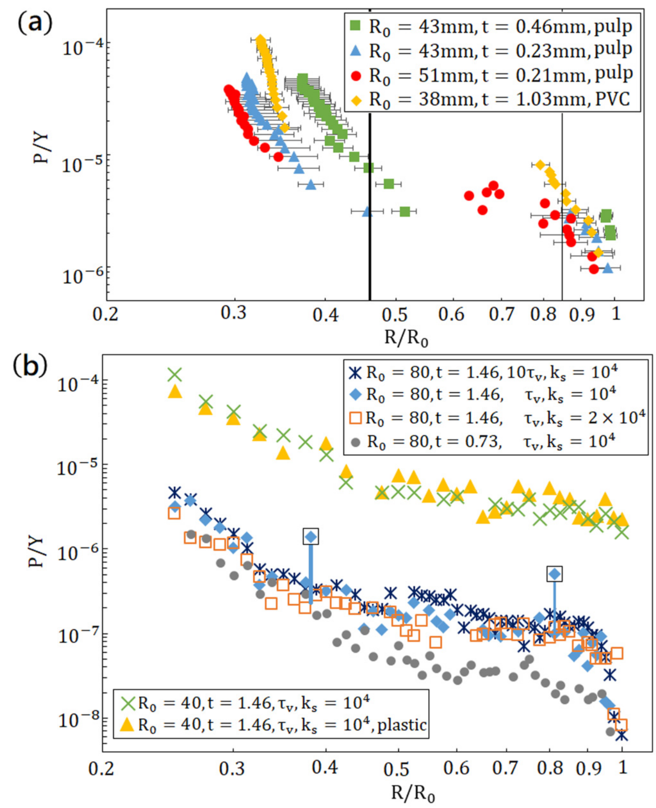


FIG. 2. The relation between $P/Y$ and $R/R_0$ for a compressed spherical shell from experiments and simulations is plotted in (a) and (b), respectively. Vertical lines signalize the boundary between different regimes. The power law in Regime 1 is fit with exponent $\alpha \sim 4.6$ and 11 for pulp and PVC balls in (a), compared to $\alpha \sim 4.78$ for blue squares in (b). The pressure for PVC balls was divided by 1000 in order to fit in panel (a).

with a smooth rim appear on the surface, as in Fig. 1(c). With further crumpling, the shell size shrinks and craters increase in number. The originally separated craters start to touch each other and their shape distorts and becomes polygonlike, which is revealed in Fig. 1(d). In this Regime 2, the response curve is flattened in Fig. 2(a), breaking away from power-law behavior. As $R/R_0 < 0.50$, a third kind of behavior is observed where the curve suddenly bends upward. We analogize this final Regime 3 to the behavior of a flat sheet [13] in a similarly compact state. However, as shown in Fig. 2(a) and unlike flat sheets, different data sets cannot be collapsed onto a master curve.

## IV. SIMULATIONS

In conjunction with experiments, we performed simulations to investigate the distributions of strains and their associated energies. The Weeks-Chandler-Anderson potential [27] is used to model the excluded volume of each lattice point in our simulations [11,28]. It defines the length unit $\sigma$ and the energy unit $\epsilon$. We follow the convention of previous simulations [11,16,28,29] by adopting a hexagonal lattice with mean spacing $L_0 = 1.0\sigma$. As discussed in Refs. [30–32], it is generally not possible to arrange lattice points regularly on a spherical surface. We have thus checked that defects with five or seven neighbors are less than 2% to safeguard the credibility of simulation. But will these defects completely alter the distribution of strains or dominate them? To reassure ourselves, we measured the stored energy in any crater that contains defects and compared it to that of a normal one. It turns out that their magnitudes are comparable [24]. A similar geometric defect also occurs when we simulate the cube and cylinder-zigzag boundaries at some edges, as shown in Sec. VII. Their number is controlled to be less than 0.5%.

Crumpling is effectuated by reducing radius $R$ of an impenetrable wall. The effective thickness $t$ of a shell is calculated from $k_b/k_s = 3t^2/32$, where $k_b$ and $k_s$ denote the bending and stretching moduli [16]. We study $t$ ranging between 0.73 and $1.46\sigma$ by varying $k_s$ from $10^4$ to $2 \times 10^4\epsilon/\sigma^2$. Different materials are simulated by varying $k_s$, while keeping $k_b/k_s$ fixed. Young's modulus is defined as $k_s/t$. The elastic energy comprises stretching, $E_s = k_s(L - L_0)^2/2$, and bending energies, $E_b = k_b(\theta - \theta_0)^2/2$, where $L$ is the length between adjacent beads, $\theta$ is the angle spanned by three consecutive beads along a lattice direction, and $\theta_0$ is the equilibrium angle. Plasticity is included by halving the magnitude of $k_b$ beyond a yield angle $|\theta - \theta_0|$ of $10^\circ$ [33]. The compression rate is set to $\tau_v = -0.001(m/\epsilon)^{-1/2}$, where $m$ is the mass of the bead. All simulations are performed using LAMMPS version 16Mar18 [34].

Simulation results are presented in Fig. 2(b), where $k_s$, $\tau_v$, $R_0$, and $t$ are varied. The curves show similar trends to Fig. 2(a). We find that a faster $\tau_v$, a smaller $R_0$, or an increase in $t$ demands a stronger pressure to reach the same crumpled state $R/R_0$. Note that a larger $P$ is also called for when the hardness is increased. A smaller shell can be viewed as a shorter spring that needs a higher pressure to crumple.

The exponent $\alpha$ was found to increase as the shell becomes larger, thinner, or softer. The same effect is also found for more plasticity and a slower $\tau_v$. Overall, the shell data give $\alpha = 4.22$–$5.01$, which is smaller than 6 for a flat sheet in simulation [11,28], 6.2 for a flat sheet made of our pulp, 7.1 for aluminum foil, and 12.0 for HDPE [13]. More information can be found in the SM. It is worth remembering that the validity of the power law is judged by the range of $P$ that experimentalists control, not $R$. However, the fact that $P$ in Fig. 2 is still less than one order and its $R$-squared value is less than 0.6 casts doubt on the assertion of a power law. We were obliged to investigate this issue since it is a renounced property for flat sheets.

Overall, a compression pressure about 1.5 times higher than that for a flat sheet of similar size is required for shells. Experiments and simulations agreed that the regime boundaries in Fig. 2 occur earlier than flat sheets [13]. Representative snapshots and cross-sections for Regimes 1, 2, and 3 are given in Fig. 3. From (a)–(c) we see that craters gradually encounter each other and their indentations deepen. Finally, the hollowed ball becomes more compact, as shown by (d)–(i). Note that radial and azimuthal distributions in (j) and (k) reveal an inhomogeneous morphology even at $R/R_0 = 0.3$.

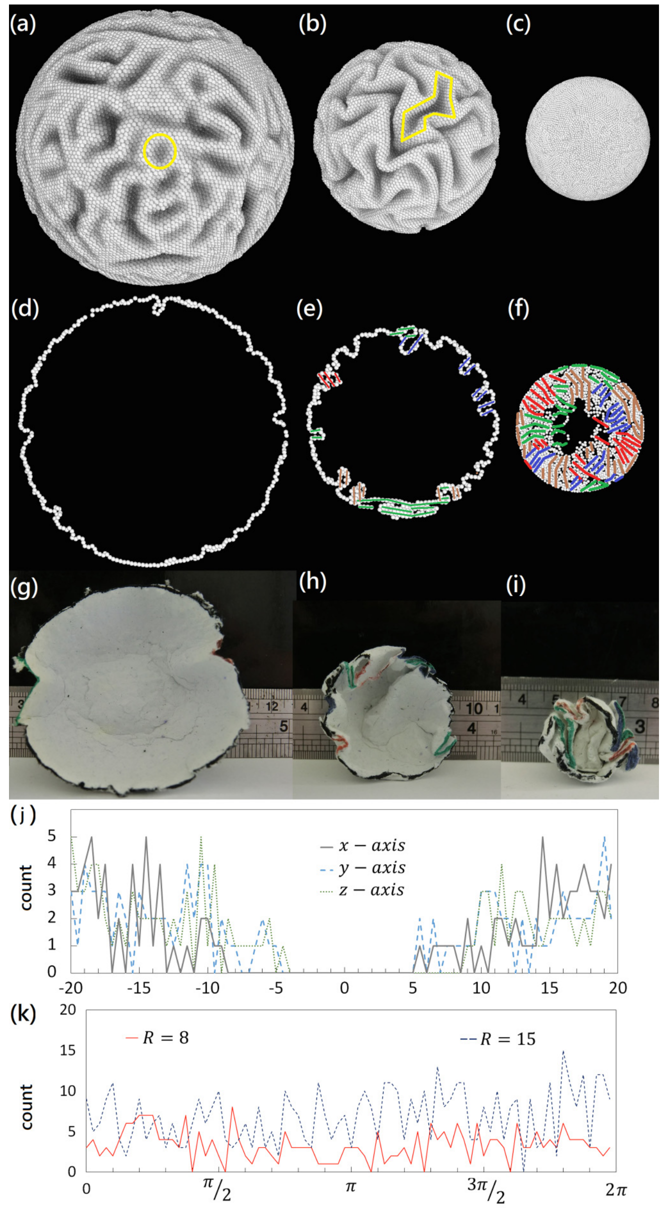


FIG. 3. The exterior of a simulated crumpled shell with $R_0 = 80$, $t = 1.46$, $0.1\tau_v$, and $k_s = 10^4$ is shown in plots (a)–(c) as $R/R_0 = 0.95$, 0.76, and 0.3. Plots (d)–(f) show the great-circle cross-section of (a)–(c) [35]. Segments are painted with the same color if their inclination angle is within $\pm 22.5^\circ$. Photos in (g)–(i) show the real sample. Density distribution is plotted in plots (j) and (k) with bin size $(0.02, 0.05\pi)$ along the $x$, $y$, and $z$ axes and the azimuthal direction at radius 8, 15 when $R/R_0 = 0.3$.

## V. ENERGETIC RESPONSE

The energetic competition can be studied by $E_b/E_s$ against $R/R_0$ in Fig. 4(a). The curve shows three characteristic behaviors: a dip in Regime 1, a mount in Regime 2, and a descent in Regime 3. As crumpling starts, the rim gets bigger while craters remain shallow. It leads to a decrease in the ratio because the dominant energy on the rim is $E_s$, which grows linearly with perimeter $\ell$; see Fig. 4(b). As the crater number increases and saturates, the system enters Regime 2. Further crumpling deepens the craters and causes an increase in $E_b$ that is proportional to the base area; see Fig. 4(c). As a result, $E_b/E_s$ increases. When the crumpled shell becomes compact in Regime 3, there is no more space for the base area to extend. This explains why $E_s$ regains its importance and renders a

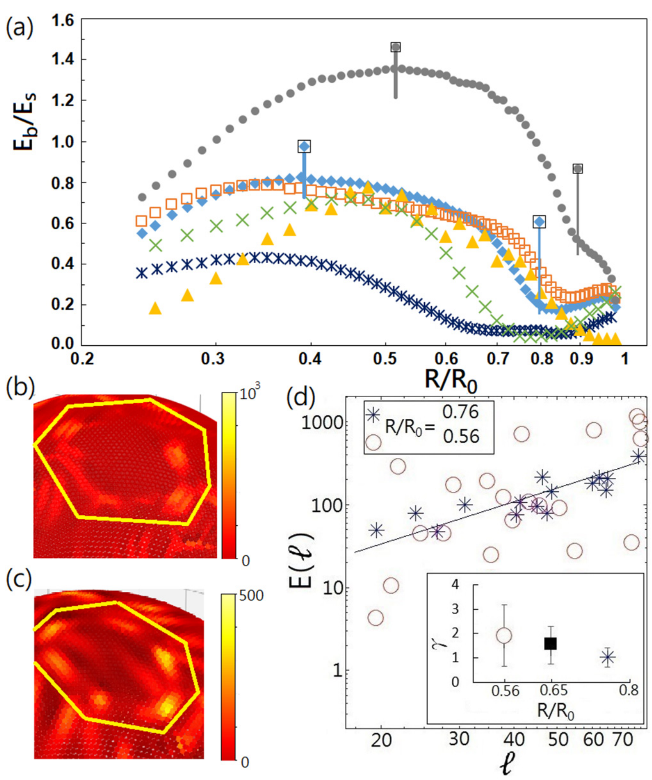


FIG. 4. Plot (a) shows $E_b/E_s$ vs $R/R_0$ for a sphere with different $R_0$, $t$, $\tau_v$, $k_s$, and plasticity, where the label follows that of Fig. 2(b). Plots (b) and (c) show the contour maps for $E_s$ and $E_b$ from simulations for $R_0 = 40$, $t = 1.46$, $\tau_v$, and $k_s = 10^4$ at $R/R_0 = 0.75$, which just enters Regime 2. The yellow circle highlights a crater where $E_s$ is concentrated at the perimeter, while energy stored in the base area consists mainly of $E_b$. Plot (d) is fit by a linear line to reveal $E(\ell) \propto \ell^\gamma$. The inset shows that $\gamma$ increases from 1.08 to 1.94 as $R/R_0$ decreases from 0.8 to 0.5 for $R_0 = 80$, $t = 1.46$, $\tau_v$, and $k_s = 10^4$. The code can be found in [36].

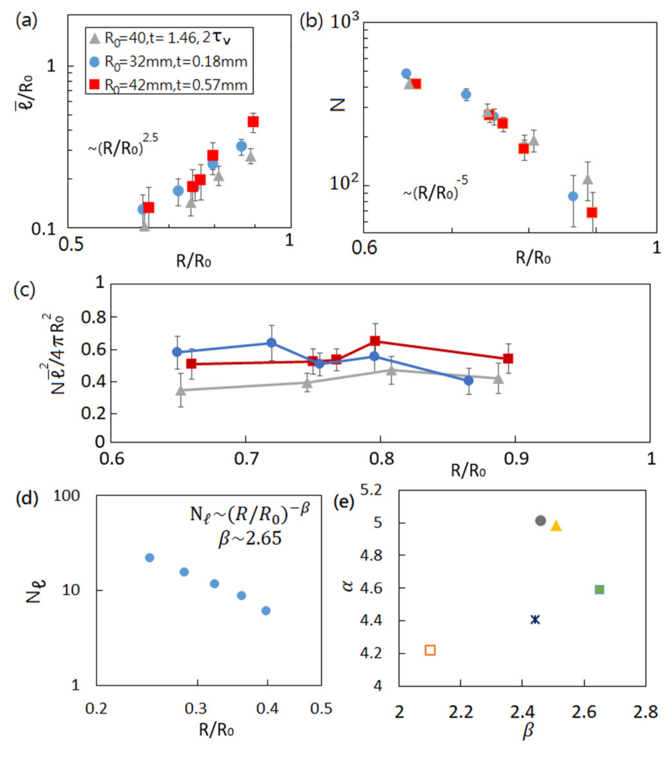


FIG. 5. Plots (a) and (b) show simulation (gray triangle) and experimental results (blue circle and red square) for $\bar{\ell}$ and $N$ vs $R/R_0$. They imply that $N\bar{\ell}^2$ remains roughly constant in plot (c). Plot (d) shows the power law for $N_\ell$ vs $R$ for $R_0 = 43$ mm and $t = 0.46$ mm. Plot (e) indicates that $\alpha$ vs $\beta$ does not follow a linear relation.

drop in $E_b/E_s$. Note that an exception is observed in Fig. 4(a) when the dip in Regime 1 disappears for a very thin shell. According to the relation $t \sim (k_b/k_s)^{1/2}$, a small $t$ signifies a stiff $k_s$. Thus, it is easier to promote $E_b$ in the deformation, which causes the dip to vanish.

Figure 4(a) also tells us that, as the shell gets thinner, bigger, harder, or with more plasticity, the transition to Regime 2 tends to happen earlier, since these properties favor a small and large number of craters. This causes craters to bump into each other earlier. A thin shell can also advance the transition to Regime 3, but a smaller and softer shell or a slower $\tau_v$ is required to achieve it. The transition happens earlier because neighboring layers can more easily line up and form ordered domains, which phase is a precursor to Regime 3. Generally speaking, Fig. 4(a) shows that the evolution of $E_b/E_s$ with $R$ for a spherical shell is more complicated than that for a flat sheet [16].

Let us now investigate how the storage energy, $E(\ell) = E_b + E_s$, of a crater increases with its perimeter $\ell$. The results for Regime 1 in Fig. 4(d) can be fit by $E(\ell) \sim \ell^\gamma$ with $\gamma \approx 1$, compared to $1/3$ in the same regime for a flat sheet. One way to understand why $\gamma < 1$ in the latter case is that all ridges exhibit vertices at both ends. So when we double the length of a ridge, no extra energy is required for the vertices whose number remains at two instead of four. In contrast, the rims of craters form a closed loop and are devoid of such vertices. As the system enters Regime 2, craters bump into each other and the smooth rims are turned into polygons. This indicates that crater-crater interactions can no longer be neglected. This breakdown of circular shape, formally called the Pogorelov state [37,38], is consistent with the prediction by Gomez *et al.* [39]. The power-law fitting becomes difficult and leads to large error bars as a result of crater-crater interactions.

## VI. STATISTICAL PROPERTIES

Now we return to the case of a sphere. Figures 5(a) and 5(b) shows the evolution of the mean length $\bar{\ell}$ and number $N$ of rims in Regime 1. The simulation results are consistent with experiments at revealing two scaling relations: $N \sim (R/R_0)^{-5}$ and $\bar{\ell}/R_0 \sim (R/R_0)^{2.5}$. When combined, they predict $N\bar{\ell}^2 \approx$ const, as in Fig. 5(c), which property is similar to a flat sheet except the latter exhibits smaller exponents at $-2$ and 1 [16]. There is an important relation between $\alpha$ and the exponent $\beta$ related to layer number, $N_\ell \sim (R/R_0)^{-\beta}$ for flat sheets [18]. Both are measured and plotted in Figs. 5(d) and 5(e) for paper shells and simulated shells. They do not seem to follow the linear relation in flat sheets [18]. We believe this is because $\alpha$ only exists for $R/R_0 > 0.76$ when there is just a single layer.

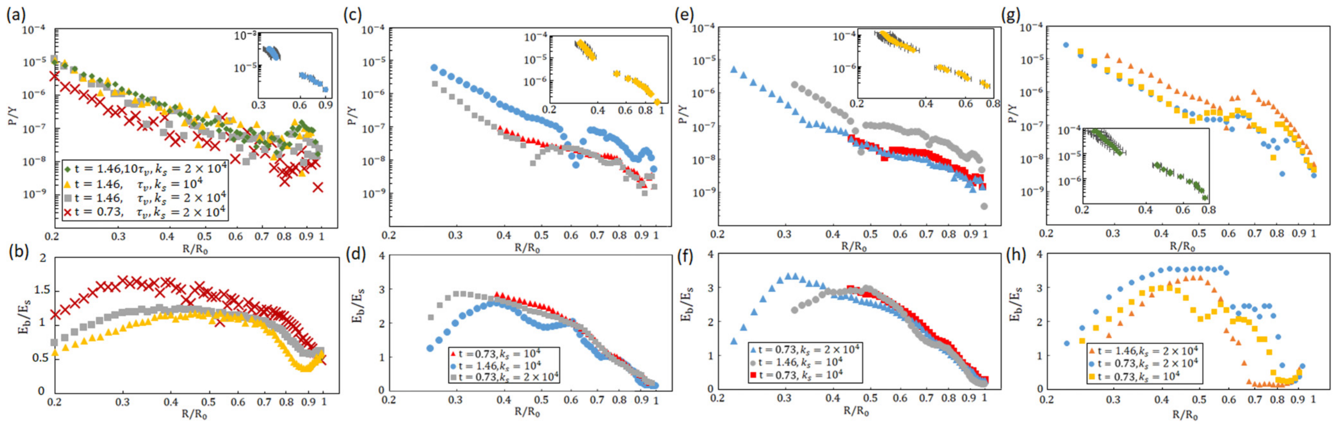

FIG. 6. The mechanical response and energetic ratio $E_b/E_s$ from simulations are shown for an elastic crumpled hemisphere with $R_0 = 80$ in (a) and (b). The same properties are also determined for a cube with $L_0 = 80$ and $R_0 \equiv \sqrt{3}L_0/2 \sim 69$ in (c) and (d), an open cube in (e) and (f), and a cylinder with transverse radius $r_0 = 30$, length $\ell_0 = 70$, and $R_0 \equiv \sqrt{(r_0)^2 + (\ell_0/2)^2} \sim 46$ in (g) and (h)—all without plasticity. Unless otherwise stated, the compression rate in the simulation is set at $\tau_v$. For contrast, consistent experimental results are shown in the insets of (a), (c), (e), and (g). The characterization of the hemisphere is $R_0 = 45$ mm, $t = 0.81$ mm, and $Y \sim 9.42 \pm 0.40$ GPa; the cube is $L_0 = 70$ mm, $t = 0.1$ mm, and $Y \sim 0.18 \pm 0.05$ GPa; and the cylinder is $r_0 = 40$ mm, $\ell_0 = 70$ mm, and $Y \sim 0.18 \pm 0.05$ GPa.

It does not overlap with the vast regime of $R/R_0 < 0.5$ where $\beta$ is determined.

By using the scaling relations in Figs. 5(a) and 5(b), storage energy $E \propto N\bar{\ell}^{\gamma}$ can be rewritten as $E \propto R^{\frac{5\gamma}{2}-5}$. Since $E$ must increase with decreasing $R$, $\gamma < 2$ is required to avoid absurdity. Pressure is then obtained as $P \propto R^{\frac{5\gamma}{2}-8}$, which prediction can be checked by Fig. 2. Power-law fitting gives $\alpha = 4.6/4.78$, which corresponds to $\gamma = 1.36/1.28$ for experiments/simulation. The fact that $\gamma$ falls within 1 and 2 is consistent with the bound determined independently by the inset of Fig. 4(d).

The evolution of $\gamma$ can be understood by realizing that there are two contributors to $E(\ell)$, i.e., $E_{\text{rim}}$ and $E_{\text{base}}$. Being proportional to $\ell$, $E_{\text{rim}}$ dominates $E_{\text{base}} \propto \ell^2$ when $\ell$ is small and increases as crumpling proceeds in Regime 1. In contrast, Regime 2 favors $E_{\text{base}}$ because it is characterized by a close pack of craters that can only grow in base area, but not the circumference. This completes our arguments for Fig. 4(d).

Armed with the knowledge of Figs. 4(b) and 4(c), we are in a better position to discuss the origin of the dip in Fig. 4(a). Separating the input to $E(\ell)$ from the base and rim informs us that $E_b/E_s \propto E_{\text{base}}/E_{\text{rim}} \propto \ell \sim R^{2.5}$. Easy differentiation gives $\frac{d(E_b/E_s)}{d(R/R_0)} \sim R^{1.5}$ with a positive coefficient. This explains why there is a dip.

## VII. HEMISPHERE, CUBE, AND CYLINDER

After revealing that many crumpling properties for a flat sheet cannot be directly applied to a sphere, we need to ask ourselves whether the difference derives from the curvature and/or dimensionality. Furthermore, other characterizations, such as the sharp edges and corners of a cube and open boundary, may also come into the equation. So further investigations are needed. The first sample we test is a hemisphere whose mechanical response turns out to be qualitatively similar to that of a full sphere except that Regime 1 is shortened even more, as shown in Fig. 6(a). This result is consistent with Fig. 1 in Ref. [40] for PDMS and the finite-element method. The extra knowledge of $E_b/E_s$ in Fig. 6(b) allows us to identify two distinct behaviors, Regimes 2 and 3. As expected, the open boundary of the hemisphere makes it easier to bend and thus renders $E_b/E_s$ almost two times higher than that of a sphere for the same compaction. As far as qualitative behavior is concerned, the open boundary appears to be irrelevant. Before eliminating it as a crucial factor, we need to smash a cubic cube with and without an open cap. As demonstrated by Figs. 6(c) and 6(d) and Figs. 6(e) and 6(f), the mechanical and energetic responses are more similar to those of a sphere than a flat sheet. However, aside from the qualitative resemblance, traces of artifact due to the sharp corners can be detected in the first bump for $E_b/E_s$, independent of whether the cube is open. With the aid of simulation, we are able to correlate the occurrence of the second bump, which is shared by Fig. 4(a) for the sphere, with the timing when deformations start to overlap or the incipient of interaction among deformations. Contrast for a real and simulated crumpled cube is provided by the photos in the SM [24]. Finally, a cylinder is crumpled out of curiosity. Imagine a Pringles cube. It sits between a sphere and a cube in that its surface exhibits a nonzero curvature only along the lateral direction; the result are shown in Figs. 6(g) and 6(h). Two bumps in $E_b/E_s$ are again obtained and caused, respectively, by the circular edges and the interaction between the extended deformations from both edges. Gathered from the above evidence that the mechanical and energetic responses of a hemisphere, a cube with or without a cap, and a cylinder are qualitatively similar to those of a sphere, we can conclude that the geometry of enclosure is the most important factor when distinguishing the crumpling of a 3D object and a flat sheet.

## VIII. CONCLUSION AND DISCUSSIONS

In conclusion, we have examined and confirmed via experiments and MD simulations that the mechanical and energetic properties of a crumpled sphere, a hemisphere, a cube, and a cylinder can be very different from those of a flat sheet, which have been extensively studied in the past. Our studies led us to conclude that the discrepancy derives mainly from the dimensionality of the sample before crumpling, rather than the existence of a nonzero curvature or/and an open boundary. The nature of deformation in two- and three-dimensional objects is drastically different: ridges and vertices versus craters. In contrast to the monotonically increasing ridge number and the decreasing ridge length, we observed that both the perimeter and the number of craters for a stereoscopic object increase initially with compaction, but they begin to decrease upon entering Regime 2 when the craters become so distorted that they cease to be discernible. The time at which (i) craters change their shape from circular to polygonal as they bump into one another coincides with two other observations: (ii) the power laws break down for $P$ versus $R$ and $E$ versus $\ell$, and (iii) $E_b/E_s$ increases suddenly. These relations can be derived for flat sheets by minimizing $E_b + E_s$ around a single isolated ridge [15]. Therefore, observations (ii) and (iii) can be viewed as an indication that the ridge-ridge interactions can no longer be ignored [16]. We believe that the same physics happens here and provides a causal link between observation (i) and observations (ii) and (iii).

In contrast to ridges, each crater consists of two components—a rim and a base. Their dominant forms of potential energy are very different, i.e., stretching and bending, respectively. The change in morphology, i.e., the spontaneous emergence of ordered domains in Regime 3, is found to be correlated with the sudden drop in the ratio of bending/stretching energies. Unlike flat sheets, mechanical and energetic responses depend sensitively on detailed parameters, such as the compression rate and the thickness, size, hardness, and degree of plasticity of the material. But what about friction, which has been proven to be critical for relaxation? To answer this question, we also ran simulations with friction, which turns out not to be crucial for the crumpling process of shells.

## ACKNOWLEDGMENTS

We gratefully acknowledge discussions and technical assistance from Sun-Ting Tsai, Yu-Min Cheng, Chi-Kang Kuo, Wei-Chi Li, and Yu-Chuan Cheng, and financial support from MoST in Taiwan under Grants No. 105-2112-M007-008-MY3 and No. 108-2112-M007-011-MY3. We are also in debt to one of the reviewers for prompting us to prioritize the importance of different sample characterizations, namely dimensionality versus curvature and open boundary, on the crumpling properties, and to determine which one is the dominant factor.

[1] J. Lidmar, L. Mirny, and D. R. Nelson, Phys. Rev. E **68**, 051910 (2003).
[2] T. Tanaka, S. T. Sun, Y. Hirokawa, S. Katayama, J. Kucera, Y. Hirose, and T. Amiya, Nature (London) **325**, 796 (1987).
[3] J. Zang, S. Ryu, N. Pugno, Q. Wang, Q. Tu, M. J. Buehler, and X. Zhao, Nat. Mater. **12**, 321 (2013).
[4] J. W. Wang and T. A. Witten, Phys. Rev. E **80**, 046610 (2009).
[5] A. Lobkovsky, S. Gentges, H. Li, D. More, and T. A. Witten, Science **270**, 1482 (1995).
[6] A. E. Lobkovsky and T. A. Witten, Phys. Rev. E **55**, 1577 (1997).
[7] Y. Kantor, M. Kardar, and D. R. Nelson, Phys. Rev. Lett. **57**, 791 (1986).
[8] K. Matan, R. B. Williams, T. A. Witten, and S. R. Nagel, Phys. Rev. Lett. **88**, 076101 (2002).
[9] A. S. Balankin, I. C. Silva, O. A. Martinez, and O. S. Huerta, Phys. Rev. E **75**, 051117 (2007).
[10] Y. Kantor and D. R. Nelson, Phys. Rev. Lett. **58**, 2774 (1987).
[11] G. A. Vliegenthart and G. Gompper, Nat. Mater. **5**, 216 (2006).
[12] Y. C. Lin, Y. L. Wang, Y. Liu, and T. M. Hong, Phys. Rev. Lett. **101**, 125504 (2008).
[13] W. B. Bai, Y. C. Lin, T. K. Hou, and T. M. Hong, Phys. Rev. E **82**, 066112 (2010).
[14] Y. C. Lin, J. M. Sun, J. H. Hsiao, Y. K. Hwu, C. L. Wang, and T. M. Hong, Phys. Rev. Lett. **103**, 263902 (2009); Y. C. Lin, J. M. Sun, H. W. Yang, Y. Hwu, C. L. Wang, and T. M. Hong, Phys. Rev. E **80**, 066114 (2009).
[15] A. J. Wood, Physica A **313**, 83 (2002).
[16] S. F. Liou, C. C. Lo, M. H. Chou, P. Y. Hsiao, and T. M. Hong, Phys. Rev. E **89**, 022404 (2014).
[17] S. Deboeuf, E. Katzav, A. Boudaoud, D. Bonn, and M. Adda-Bedia, Phys. Rev. Lett. **110**, 104301 (2013).
[18] M. Habibi, M. Adda-Bediac, and D. Bonna, Soft Matter **13**, 4029 (2017).
[19] M. C. Fokker, S. Janbaz, and A. A. Zadpoor, RSC Adv. **9**, 5174 (2019).
[20] E. van Bruggen, E. Van der Linden, and M. Habibi, Soft Matter **15**, 1633 (2019).
[21] H. Yuan, K. Wu, J. Zhang, Y. Wang, G. Liu, and J. Sun, Adv. Mater. **31**, 1900933 (2019).
[22] E. P. Degarmo, J. Black, and R. A. Kohser, *Materials and Processes in Manufacturing*, 9th ed. (Wiley, New York, 2003), p. 223.
[23] A. B. Croll, T. Twohig, and T. Elder, arXiv:1801.01166.
[24] See Supplemental Material at http://link.aps.org/supplemental/10.1103/PhysRevE.103.012209 for more data and plots.
[25] A. S. Balankin, O. S. Huerta, R. Cortes Montes de Oca, D. S. Ochoa, J. Martinez Trinidad, and M. A. Mendoza, Phys. Rev. E **74**, 061602 (2006); A. S. Balankin, R. Cortes Montes de Oca, and D. S. Ochoa, *ibid.* **76**, 032101 (2007).
[26] Consistent with Fig. 2 B in J. Shim, C. Perdigou, E. R. Chen, K. Bertoldi, and P. M. Reis, Proc. Natl. Acad. Sci. (USA) **109**, 5978 (2012), where buckyballs were crumpled until the beginning of Regime 2.
[27] J. D. Weeks, D. Chandler, and H. C. Andersen, J. Chem. Phys. **54**, 5237 (1971).
[28] T. Tallinen, J. A. Åström, and J. Timonen, Nat. Mater. **8**, 25 (2009).
[29] G. Vliegenthart and G. Gompper, New J. Phys. **13**, 045020 (2011).

[30] H. S. Seung and D. R. Nelson, Phys. Rev. A **38**, 1005 (1988).
[31] D. R. Nelson, Phys. Rev. B **28**, 5515 (1983).
[32] F. L. Jiménez, N. Stoop, R. Lagrange, J. Dunkel, and P. M. Reis, Phys. Rev. Lett. **116**, 104301 (2016).
[33] https://reurl.cc/KkpMGn
[34] S. J. Plimpton, J. Comput. Phys. **117**, 1 (1995).
[35] A. Stukowski, Modell. Simul. Mater. Sci. Eng. **18**, 015012 (2010)
[36] https://github.com/mnb11338.
[37] A. V. Pogorelov, *Bendings of Surfaces and Stability of Shells* (American Mathematical Society, Providence, RI, 1988), Vol. 72.
[38] N. P. Bende, A. A. Evans, S. Innes-Gold, L. A. Marin, I. Cohen, R. C. Hayward, and C. D. Santangelo, Proc. Natl. Acad. Sci. (USA) **112**, 11175 (2015).
[39] M. Gomez, D. E. Moulton, and D. Vella, Proc. R. Soc. A **472**, 20150732 (2016).
[40] E. Kanako, S. Yusaku, Y. Akio, Z. Liangliang, L. Xiangbiao, and C. Xi, Soft Matter **16**, 3952 (2020)